ELSEVIER

Progress in Quantum Electronics 32 (2008) 89–120

Progress in Quantum Electronics

www.elsevier.com/locate/pquantelec

Review

Quantum-dot infrared photodetectors: Status and outlook

P. Martyniuk, A. Rogalski*

Institute of Applied Physics, Military University of Technology, 2 Kaliskiego Str., 00-908 Warsaw, Poland

Abstract

This paper reviews the present status and possible future developments of quantum-dot infrared photodetectors (QDIPs). At the beginning the paper summarizes the fundamental properties of QDIPs. Next, an emphasis is put on their potential developments. Investigations of the performance of QDIPs as compared to other types of infrared photodetectors are presented. A model is based on fundamental performance limitations enabling a direct comparison between different infrared material technologies. It is assumed that the performance is due to thermal generation in the active detector's region. In comparative studies, the HgCdTe photodiodes, quantum well infrared photodetectors (QWIPs), type-II superlattice photodiodes, Schottky barrier photoemissive detectors, doped silicon detectors, and high-temperature superconductor detectors are considered.

Theoretical predictions indicate that only type-II superlattice photodiodes and QDIPs are expected to compete with HgCdTe photodiodes. QDIPs theoretically have several advantages compared with QWIPs including the normal incidence response, lower dark current, higher operating temperature, higher responsivity and detectivity. The operating temperature for HgCdTe detectors is higher than for other types of photon detectors. It is also shown, that BLIP temperature of QDIP strongly depends on nonuniformity in the QD size.

Comparison of QDIP performance with HgCdTe detectors gives clear evidence that the QDIP is suitable for high operation temperature. It can be expected that improvement in technology and design of QDIP detectors will make it possible to achieve both high sensitivity and fast response useful for practical application at room temperature FPAs.

Comparison of theoretically predicted and experimental data indicates that, as so far, the QDIP devices have not fully demonstrated their potential advantages and are expected to posses the

*Corresponding author. Tel./fax: +48 22 683 9109.
E-mail address: rogan@wat.edu.pl (A. Rogalski).

0079-6727/$ - see front matter
doi:10.1016/j.pquantelec.2008.07.001

fundamental ability to achieve higher detector performance. Poor QDIP performance is generally linked to nonoptimal band structure and controlling the QDs size and density (nonuniformity in QD size).

Keywords: Quantum-dot infrared photodetectors; Quantum well infrared photodetectors; HgCdTe photodiodes; Type-II superlattices; RA product; Detectivity

Contents

1. Introduction

Since the initial proposal by Esaki and Tsu in 1970 [1] and the advent of molecular beam epitaxy (MBE), the interest in semiconductor low-dimensional solids has increased continuously over the years, driven by technological challenges, new physical concepts and phenomena as well as promising applications. A new class of materials with unique optoelectronic properties has been developed. Zero-dimensional quantum confined semiconductor heterostructures have been investigated theoretically and experimentally for some time [2–4]. At present, nearly defect-free quantum-dot devices can be fabricated reliably and reproducibly. Also new types of infrared photodetectors taking advantage of the quantum confinement obtained in semiconductor heterostructures have been emerged.

As it was indicated by Kinch [5], photon detectors can be divided into two broad classes, namely majority and minority carrier devices. We can distinguish six infrared (IR) material systems:

1. Direct bandgap semiconductors—minority carriers
   - binary alloys: InSb, InAs
   - ternary alloys: HgCdTe, InGaAs
   - type-II, -III superlattices: InAs/GaInSb, HgTe/CdTe
2. Extrinsic semiconductors—majority carriers
   - Si:As, Si:Ga, Si:Sb
   - Ge:Hg, Ge:Ga
3. Type-I superlattices—majority carriers
   - GaAs/AlGaAs QWIPs
4. Silicon Schottky barriers—majority carriers
   - PtSi, IrSi
5. Quantum dots—majority carriers
   - InAs/GaAs QDIPs
6. High-temperature superconductors (HTSC)—minority carriers

All of these material systems have been seriously players in the IR marketplace with the exception of the HTSC and quantum-dot infrared photodetectors (QDIPs). The dates given in Fig. 1 show the chronology of significant development efforts on the materials mentioned. First observations of intersublevel transitions in the far IR were reported in the early 1990s, either in InSb-based electrostatically defined quantum dots [6] or in structured

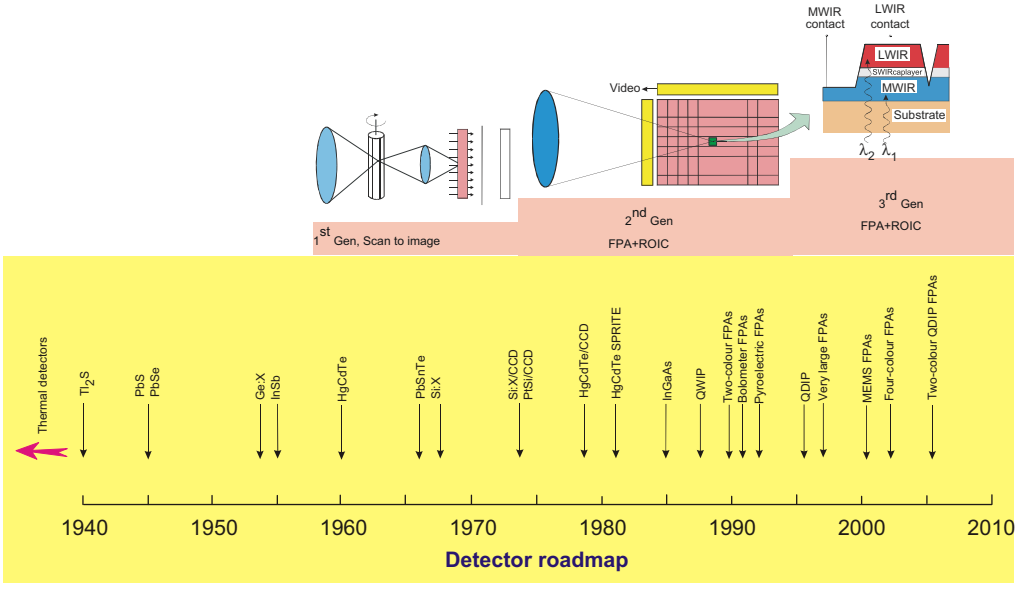

Fig. 1. History of the development of infrared detectors and systems. Three generation systems can be considered for principal military and civilian applications: first generation (scanning systems), second generation (staring systems—electronically scanned) and third generation (multicolour functionality and other on-chip functions).

two-dimensional (2-D) electron gas [7]. The first QDIP was demonstrated in 1998 [8]. Ever since great progress has been made in their development and performance characteristics [9,10] and in their applications to thermal imaging focal plane arrays (FPA) [11].

The beginning of the interest in quantum-dot research can be traced back to a suggestion by Arakawa and Sakaki in 1982 [2] that the performance of semiconductor lasers could be improved by reducing the dimensionality of the active regions of these devices. Initial efforts at reducing the dimensionality of the active regions focused on using ultrafine lithography coupled with wet or dry chemical etching to form 3-D structures. It was soon realized, however, that this approach introduced defects (high density of surface states) that greatly limited the performance of such quantum dots. Initial efforts were mainly focused on the growth of InGaAs nanometer-sized islands on GaAs substrates. In 1993, the first epitaxial growth of defect-free quantum-dot nanostructures was achieved by using MBE [12]. Most of the practical quantum-dot structures today are synthesized both by MBE and MOCVD.

Under certain growth conditions, when the thickness of the film with the larger lattice constant exceeds a certain critical thickness, the compressive strain within the film is relieved by the formation of coherent island. These islands may be quantum dots. Coherent quantum-dot islands are generally formed only when the growth proceeds in what is known as Stranski–Krastanow growth model [13]. The onset of the transformation of the growth process from a 2-D layer-by-layer growth mode to a 3-D island growth mode results in a spotty RHEED pattern. This is, in contrast to the conventional streaky pattern, generally observed for the layer-by-layer growth mode. The transition typically occurs after the deposition of a certain number of monolayers. For InAs on GaAs, this transition occurs after about 1.7 monolayers of InAs have been grown; this is the onset of islanding and, hence, quantum-dot formation.

The most advanced III–V IR detectors, which utilize intersubband or subband to continuum transitions in quantum wells, are GaAs/AlGaAs quantum well infrared photodetectors (QWIPs). The imaging performance of FPA fabricated with this material system is comparable to the state of art of HgCdTe [14,15].

This paper summarizes the fundamental properties of QDIPs. The intent is to concentrate on device approaches and present stage of development. A secondary aim is to compare the potential QDIP performance with different material systems used in IR detector technology. Our intention is to concentrate on fundamental phenomena and minimize any confusion that might exist within the minds of scientists. The paper completes two previously published papers by Kinch [5] and Phillips [16].

2. Anticipated advantages of QDIPs

The success of quantum well structures for IR detection applications has stimulated the development of QDIPs. In general, QDIPs are similar to QWIPs but with the quantum wells replaced by quantum dots, which have size confinement in all spatial directions.

Fig. 2 shows the schematic layers of a QWIP and a QDIP. In both cases, the detection mechanism is based on the intraband photoexcitation of electrons from confined states in the conduction band wells or dots into the continuum. The emitted electrons drift towards the collector in the electric field provided by the applied bias, and photocurrent is created. It is assumed, that the potential profile at the conduction band edge along the growth

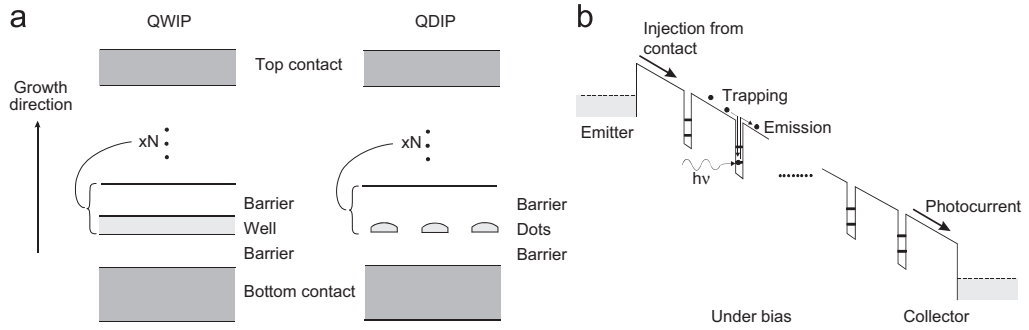

Fig. 2. Schematic layers of QWIP and QDIP (a) and potential profile for both structures under bias (b). For QDIP, influence of wetting layer is neglected (after Ref. [17]).

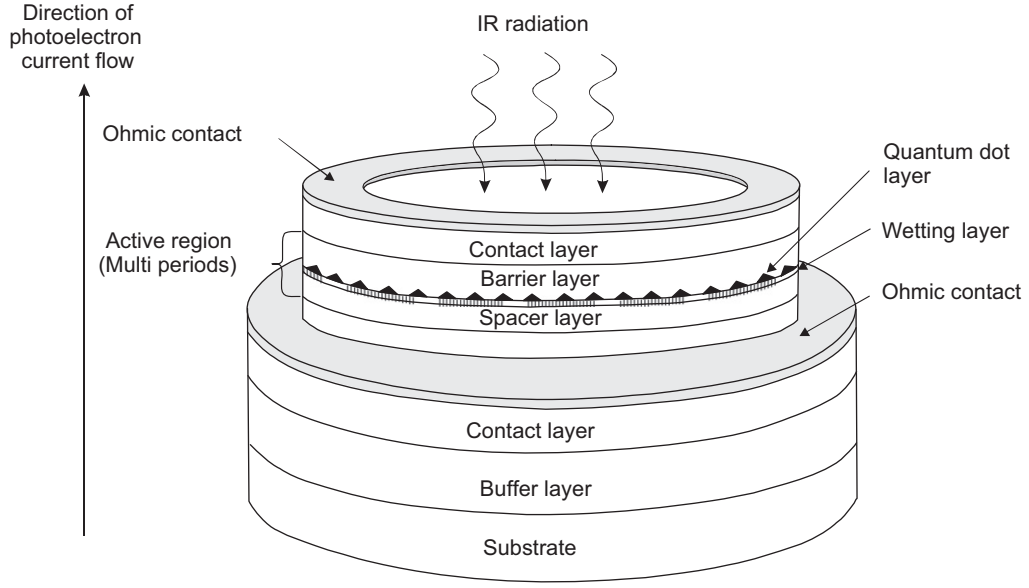

Fig. 3. Schematic diagram of conventional quantum-dot detector structure.

direction for both structure have a similar shape as shown in Fig. 2(b). In practice, since the dots are spontaneously self-assembled during growth, they are not correlated between multilayers in active region.

Two types of QDIP structures have been proposed: conventional structure (vertical) and lateral structure. In a vertical QDIP, the photocurrent is collected through the vertical transport of carriers between top and bottom contacts (see Fig. 3). The device heterostructure comprises repeated InAs QD layers buried between GaAs barriers with top and bottom contact layers at active region boundaries. The mesa height can vary from 1 to 4 μm depending on the device heterostructure. The quantum dots are directly doped (usually with silicon) in order to provide free carriers during photoexcitation, and an AlGaAs barrier can be included in the vertical device heterostructure in order to block dark current created by thermionic emission [18,19].

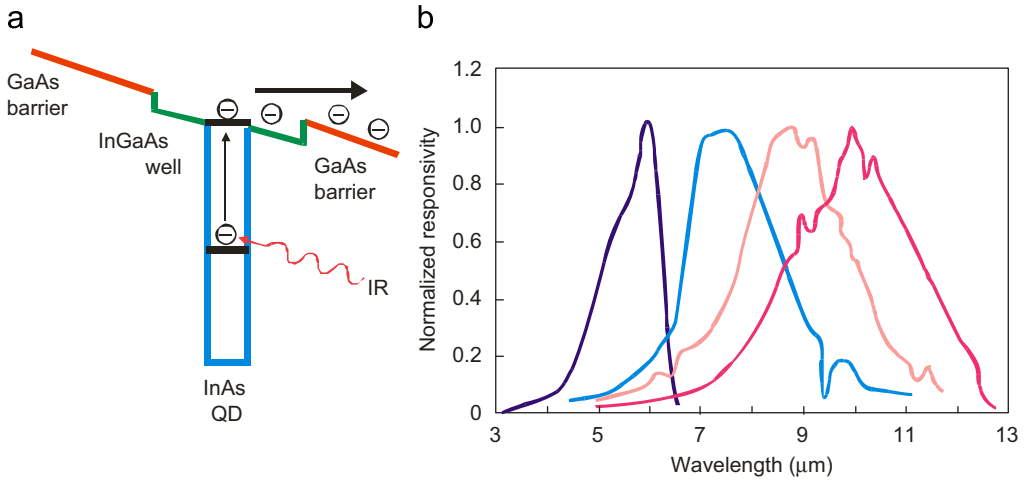

Fig. 4. DWELL infrared detector: (a) the operation mechanism, (b) experimentally measured spectral tunability by varying well width from 55 to 100 Å (after Ref. [21]).

In addition to the standard InAs/GaAs QDIP, several other heterostructure designs have been investigated for use as IR photodetectors [9,10]. An example is InAs QDs embedded in a strain-relieving InGaAs quantum well which are known as dot-in-a-well (DWELL) heterostructures (see Fig. 4) [11,20]. This device offers two advantages: challenges in wavelength tuning through dot-size control can be compensated in part by engineering the quantum well sizes, which can be controlled precisely and quantum wells can trap electrons and aid in carrier capture by QDs, thereby facilitating ground state refilling. Fig. 4(b) shows DWELL spectral tuning by varying well geometry.

The lateral QDIP collects photocurrent through transport of carriers across a high-mobility channel between two top contacts, operating much like a field-effect transistor. As previously, again AlGaAs barriers are present, but instead of blocking the dark current, these barriers are used to both modulation-dope the quantum dots and to provide the high-mobility channel. Lateral QDIPs have demonstrated lower dark currents and higher operating temperatures than vertical QDIPs since the major components of the dark current arise from interdot tunnelling and hopping conduction [22]. However, these devices will be difficult to incorporate into a FPA hybrid-bump bonded to a silicon readout circuit. Because of this, more efforts is directed to improve the performance of vertical QDIPs, which are more compatible with commercially available readout circuits.

The quantum-mechanical nature of QDIPs leads to several advantages over QWIPs and other types of IR detectors that are available. As in the HgCdTe, QWIP and type-II superlattice technologies, QDIPS provide multi-wavelength detection. However, QDs provide many additional parameters for tuning the energy spacing between energy levels, such as QD size and shape, strain, and material composition.

The potential advantages in using QDIPs over quantum wells are as follows:

- Intersubband absorption may be allowed at normal incidence (for n-type material). In QWIPs, only transitions polarized perpendicularly to the growth direction are allowed,

due to absorption selection rules. The selection rules in QDIPs are inherently different, and normal incidence absorption is observed.

- Thermal generation of electrons is significantly reduced due to the energy quantization in all three dimensions. As a result, the electron relaxation time from excited states increases due to phonon bottleneck. Generation by LO phonons is prohibited unless the gap between the discrete energy levels equals exactly to that of the phonon. This prohibition does not apply to quantum wells, since the levels are quantized only in the growth direction and a continuum exists in the other two directions (hence generation-recombination by LO phonons with capture time of few picoseconds). Thus, it is expected that S/N ratio in QDIPs will be significantly larger than that of QWIPs.
- Lower dark current of QDIPs is expected than of HgCdTe detectors and QWIPs due to 3-D quantum confinement of the electron wavefunction.

Both the increased electron lifetime and the reduced dark current indicate that QDIPs should be able to provide high-temperature operation. In practice, however, it has been a challenge to meet all of above expectations.

Carrier relaxation times in QDs are longer than the typical 1–10 ps measured for quantum wells. It is predicted that the carrier relaxation time in QDs is limited by electron–hole scattering [23], rather than phonon scattering. For QDIPs, the lifetime is expected to be even larger, greater than 1 ns, since the QDIPs are majority carrier devices due to absence of holes.

The main disadvantage of the QDIP is the large inhomogeneous linewidth of the quantum-dot ensemble variation of dot size in the Stranski–Krastanow growth mode [16,24]. As a result, the absorption coefficient is reduced, since it is inversely proportional to the ensemble linewidth. Large, inhomogeneously broadened linewidth has a deleterious effect on QDIP performance. Subsequently, the quantum efficiency QD devices tend to be lower than what is predicted theoretically. Vertical coupling of quantum-dot layers also reduces the inhomogeneous linewidth of the quantum-dot ensemble; however, it may also increase the dark current of the device, since carriers can tunnel through adjacent dot layers more easily. As in other type of detectors, also nonuniform dopant incorporation adversely affects the performance of the QDIP. Therefore, improving QD uniformity is a key issue in the increasing absorption coefficient and improving the performance. Thus, the growth and design of unique QD heterostructure is one of the most important issues related to achievement of state-of-the art QDIP performance.

3. Performance limits of infrared photodetectors

The total generation rate of IR detector is a sum of the optical and thermal generation

$$G = G_{\mathrm{th}} + G_{\mathrm{op}}. \tag{1}$$

The optical generation may be due to the signal or background radiation. For IR detectors, usually background radiation is higher compared to the signal radiation. If the thermal generation is reduced much below the background level, the performance of the device is determined by the background radiation (BLIP conditions for background limited IR photodetector). This condition can be described as [5]

$$\frac{\eta \Phi_{\mathrm{B}} \tau}{t} > n_{\mathrm{th}}, \tag{2}$$

where n_{th} is the density of thermal carriers at the temperature T, τ is the carrier lifetime, Φ_B is the total background photon flux density (unit $cm^{-2}s^{-1}$) reaching the detector, and t is the detector's thickness. Re-arranging, we have for the BLIP requirements

$$\frac{\eta\Phi_B}{t} > \frac{n_{th}}{\tau}, \tag{3}$$

i.e., the photon generation rate per unit volume needs to be greater than the thermal generation rate per unit volume. The carriers can be either majority or minority in nature. Using $\eta = \alpha t$, where α is the absorption coefficient in the material, we obtain

$$\Phi_B > \frac{n_{th}}{\alpha\tau} = G_{th}. \tag{4}$$

The normalized thermal generation, $G_{th} = n_{th}/(\alpha\tau)$, predicts the ultimate performance of any IR material and can be used to compare the relative performance of different materials as a function of temperature and energy gap (cutoff wavelength).

It should be noted that the importance of the thermal generation rate as a material figure of merit was recognized for the first time by Long [25]. It was used in many papers by English workers [26,27] related to high operating temperature (HOT) detectors. Eq. (4) was introduced by Kinch [5], which is the thermal generation rate within $1/\alpha$ depth per unit of area, as the figure of merit. This formula is actually the inverse α/G_{th} figure of merit previously proposed by Piotrowski and Gawron [28].

In further considerations we use a simple set of fundamental detector parameters described in excellent Kinch's paper [5] to compare the performance of different material systems used in IR detector technology. In the case of QDIPs, a model developed by Phillips is adapted [16].

3.1. QDIP model

Fig. 5 shows a schematic view of the QDIP structure under considerations. Simple estimation indicates that the quantum-dot density $\delta = 1/s^2$, where s is the interdot spacing. We will consider a planar array of quantum dots with conduction band structure containing two confined energy levels (E_1 and E_2) and the excited state transition coinciding with the barrier conduction band minimum.

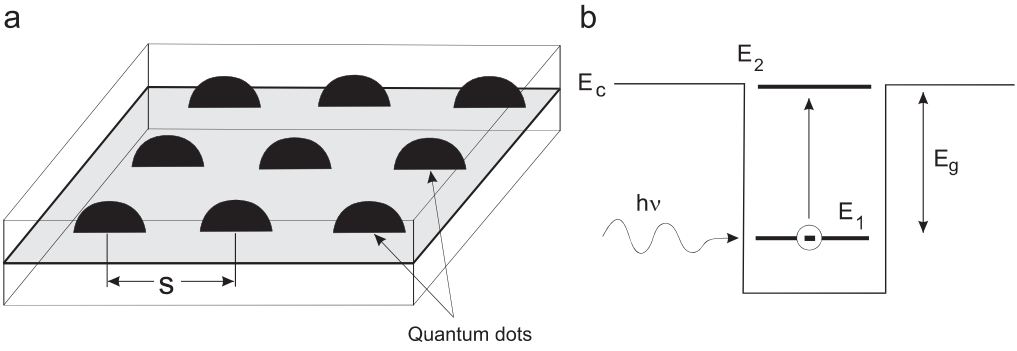

Fig. 5. Schematic view of the quantum-dot array (a) and conduction band structure of the dot (b) (after Ref. [16]).

Due to discrete nature of QDs, the fill factor F should be included for optical absorption in quantum dots. This factor can be estimated in a simple way as

$$F = \frac{\sqrt[3]{V}}{s}, \tag{5}$$

where V is the quantum-dot volume.

For self-assembled QDs, a Gaussian distribution has been observed for the electronic and optical spectra. Phillips modelled the absorption spectra for an ensemble of QDs using a Gaussian line shape in the shape

$$\alpha(E) = \alpha_o \frac{n_1}{\delta} \frac{\sigma_{QD}}{\sigma_{ens}} \exp\left[-\frac{(E - E_g)^2}{\sigma_{ens}^2}\right], \tag{6}$$

where α_o is the maximum absorption coefficient, n_1 is the areal density of electrons in the quantum-dot ground state, δ is the quantum-dot density, and $E_g = E_2 - E_1$ is the energy of the optical transition between ground and excited states in the QDs. The expressions σ_{QD} and σ_{ens} are the standard deviations in the Gaussian line shape for intraband absorption in a single quantum dot and for the distribution in energies for the QD ensemble, respectively. It should be noticed that Eq. (6) estimates the absorption coefficient for the necessary presents of electrons in the QD ground state. The terms n_1/δ and σ_{QD}/σ_{ens} describe a decrease in absorption due to absence of available electrons in the QD ground state and inhomogeneous broadening, respectively.

To calculate thermal distribution of carrier density, the Fermi distribution is used. Then, the electron densities in the QD sheet for the energy level n is given by

$$n_n = \int \frac{g\delta}{\sqrt{\pi}\sigma} \exp\left[-\frac{(E - E_n)^2}{\sigma^2}\right] f(E_n)\,dE, \tag{7}$$

where g is the degeneracy factor for the energy level, E_n is the mean energy, σ is the standard deviation in energy for the Gaussian line shape (to describe the spread of QD energy levels, again a Gaussian distribution with standard deviation σ is used [29]). Because, however, $\sigma < E_g = E_2 - E_1$, the Gaussian line shape function describing carrier densities in QD ground and excited states has little effect, and then Eq. (7) can be simplified to

$$n_n = g\delta F(E_n). \tag{8}$$

Next, taking into account the charge neutrality condition, the 2-D carrier densities may be given by

$$N_d = n_1 + n_2 + n_b = 2\delta f(E_1) + 8\delta f(E_2) + \int_0^\infty g^{2D}(E) f(E_c)\,dE, \tag{9}$$

where N_d is the sheet density dopant level. We assume a degeneracy of $g = 2$ (two-spin states) for the QD ground state, and $g = 8$ (fourfold degeneracy and two-spin state each [30]) for the quantum-dot excited state. As it was mentioned previously, the excited state coincides with the conduction band minimum of the barrier material; $E_c = E_2$. Then, the thermal carrier density is $n_2 + n_b$, where n_b is the carrier density in the conduction band.

3.2. Normalized dark current

The normalized dark current density, given by $G_{th}q$, is presented as [see Eq. (4)]

$$J_{dark} = G_{th}q = \frac{q\sigma\delta t}{\alpha_o n_1 F\tau}(n_2 + n_b). \tag{10}$$

In the calculation we assume the material parameters chosen by Phillips [16]: $\alpha_o = 5\times10^4\,cm^{-2}$, $V = 5.3\times10^{-19}\,cm^{-3}$, $\delta = 5\times10^{10}\,cm^{-2}$, $\tau = 1\,ns$, $N_d = 1\times10^{11}\,cm^{-2}$ and the detector thickness $t = 1/\alpha_o$. These parameters are representative for self-assembled InAs/GaAs quantum dots reported in the literature. The dopand concentration corresponds to two electrons per QD. In further analysis, for clarity, we assume that inhomogeneous broadening of the dot ensemble is neglected ($\sigma_{QD}/\sigma_{ens} = 1$).

The normalized dark current densities for the various materials used in IR detector technologies in LWIR spectral region ($E_g = 0.124\,eV$, $\lambda_c = 10\,\mu m$) are shown in Fig. 6. In addition, the $f/2$ background flux current density is also shown. The extrinsic silicon, the HTSC and the photoemissive (silicon Schottky barrier) detectors are hypothetical, but are included for comparison. In the calculations, carried out for different material systems we have followed the procedures used in Kinch's paper [5] (see Appendix), except QDIPs where the Phillips' model is used [16].

In the MWIR and LWIR regions, the dominant position have HgCdTe photodiodes. QWIPs are mainly used in LWIR tactical systems operating at lower temperature, typically 65–70 K, where cooling is not an issue. Large detector arrays with more than one million detector elements are fabricated by several manufacturers using these material systems. Beyond 15 μm, good performance is achieved using extrinsic silicon detectors. These detectors are termed impurity band conduction (IBC) detectors and found niche market for the astronomy and civil space communities because HgCdTe has not yet realized its potential at low temperatures and reduced background.

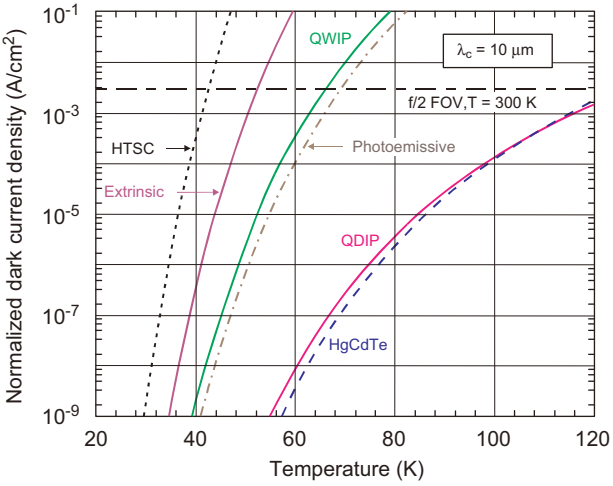

Fig. 6. Temperature dependence of the normalized dark current of various LWIR material technologies. The $f/2$ background flux current density is also shown.

Fig. 6 displays that tuneable bandgap alloy, HgCdTe, demonstrates the highest performance (the lowest dark current/thermal generation and the highest BLIP operating temperature). These estimations are confirmed by experimental data [31,32]. For very uniform QD ensembles, the QDIP performance can be close to HgCdTe one and potentially can exceeds that of HgCdTe in the region of high operation temperatures.

3.3. Detectivity

The normalized dark current, $J_{\text{dark}} = G_{\text{th}}q$, directly determines thermal detectivity

$$D^* = \frac{\eta}{qhv\sqrt{2G_{\text{th}}}}. \tag{11}$$

Fig. 7 compares the thermal detectivties of various photodetectors with cutoff wavelength in MWIR ($\lambda_c = 5\,\mu\text{m}$) and LWIR ($\lambda_c = 10\,\mu\text{m}$) regions. The assumed typical quantum efficiencies are indicated in the figure. Theoretical estimations for QDIPs are carried out assuming low quantum efficiency $\approx 2\%$ (often measured in practice) and 67%. The last value is typical for HgCdTe photodiodes (without antireflection coating). It should be noticed, however, that rapid progress has recently been made in the performance of QDIP devices, especially at near-room temperature. Lim et al. have announced a quantum efficiency of 35% for detectors with peak detection wavelength around 4.1 μm [33].

Estimation of detectivity for InAs/GaInSb strained layer superlattices (SLSs) are based on several theoretical papers published previously [34–38]. Early calculations showed that a LWIR type-II InAs/GaInSb SLS should have an absorption coefficient comparable to an HgCdTe alloy with the same cutoff wavelength [34]. Fig. 7(b) predicts that type-II superlattices are the most efficient detector of IR radiation in long-wavelength region. It is even better material than HgCdTe; it is characterized by high absorption coefficient and relatively low thermal generation rate. However, hitherto, this theoretical prediction has been not confirmed by experimental data. The main reason of that is influence of

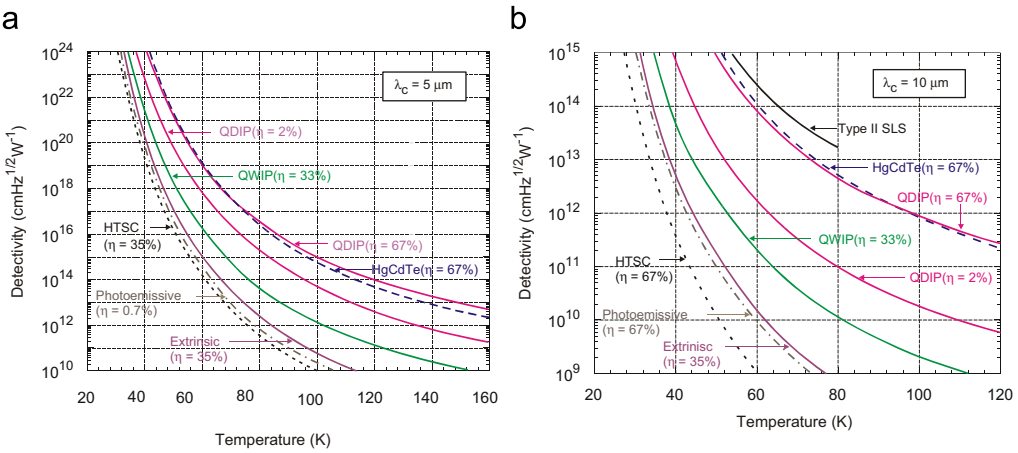

Fig. 7. The predicted thermal detectivity versus temperature for various MWIR ($\lambda_c = 5\,\mu\text{m}$) (a) and LWIR ($\lambda_c = 5\,\mu\text{m}$) (b) photodetectors. The assumed quantum efficiencies are indicated.

Schockley–Read generation-recombination mechanism, which causes lower carrier lifetime (higher thermal generation rate). It is clear from this analysis that the fundamental performance limitation of QWIPs is unlikely to rival HgCdTe photodetectors. However, the performance of very uniform QDIP [when $\sigma_{ens}/\sigma_{QD} = 1$, see Eq. (6)] is predicted to rival with HgCdTe. We can also notice from Fig. 7 that AlGaAs/GaAs quantum well infrared photoconductor (QWIP) is better material than extrinsic silicon.

3.4. BLIP temperature

BLIP temperature is defined that the device is operating at a temperature at which the dark current is equal to the background photocurrent, given a field of view (FOV) and a background temperature.

In Fig. 8(a), plots of the calculated temperature required for background limited (BLIP) operation in $f/2$ FOV are shown as a function of cutoff wavelength for various types of detectors. We can see that the operating temperature of QDIPs is comparable with HgCdTe photodiodes. HgCdTe detectors with background limited performance operate in practice with thermoelectric coolers in the MWIR range, but the LWIR detectors ($8 \leqslant \lambda_c \leqslant 12\,\mu m$) operate at $\approx 100\,K$. HgCdTe photodiodes exhibit higher operating temperature compared to extrinsic detectors, silicide Schottky barriers, QWIPs and HTSCs. Type-II SLSs are omitted in our considerations. The cooling requirements for QWIPs with cutoff wavelengths below 10 μm are less stringent in comparison with extrinsic detectors, Schottky barrier devices, and HTSCs.

Fig. 8(b) gives additional insight on influence of QD nonuniformity on BLIP temperature. The quantum efficiency for QWIPs, equal to 50%, has been assumed since QWIP cannot detect normal incidence radiation. It has been shown by Phillips [16] that the detector performance may be degraded by orders of magnitude for the values of $\sigma_{ens}/\sigma_{QD} = 100$, which are indicative of the current state of QD fabrication technology. It is well known, that reduced optical absorption in QDs due to size nonuniformity results in an increase in the normalized dark current and a reduction in detectivity.

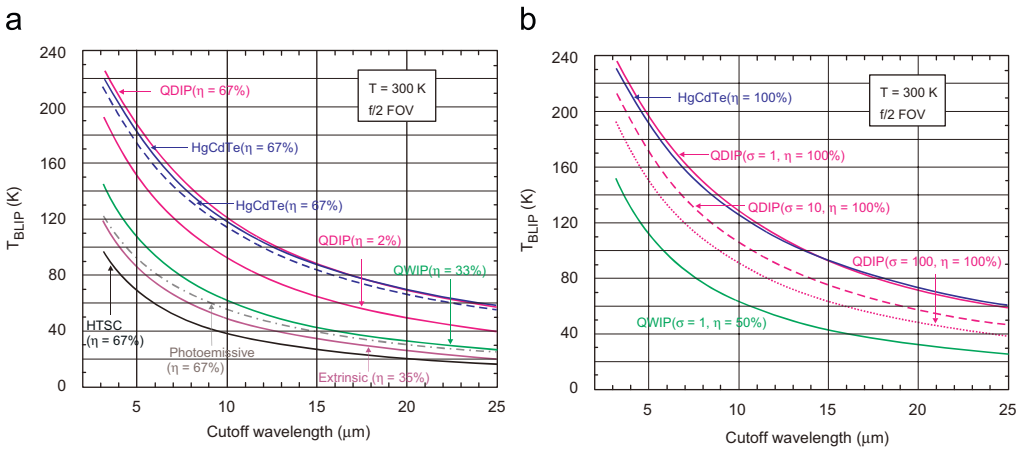

Fig. 8. Estimation of the temperature required for background-limited operation of: (a) various types of photodetectors and (b) QDIPs with different levels of quantum-dot size nonuniformity.

The nonuniformity has also strong influence on BLIP temperature. Increase of σ_{ens}/σ_{QD} ratio from 1 to 100 causes decrease of T_{BLIP} by several tens of degrees.

4. QDIPs vs. HgCdTe photodiodes

HgCdTe ternary alloy is nearly ideal IR detector material system and is the most widely used variable-gap semiconductor for IR photodetectors. Its position is conditioned by three key features [31,32]:

- tailorable energy band gap over the 1–30-μm range,
- large optical coefficients that enable high quantum efficiency, and
- favourable inherent recombination mechanisms (relatively low thermal generation rate) that lead to HOT.

These properties are direct consequence of the energy band structure of this zinc-blende semiconductor. Moreover, the specific advantages of HgCdTe are ability to obtain both low and high carrier concentrations, high mobility of electrons, and low dielectric constant. The extremely small change of lattice constant with composition makes it possible to grow high quality layered and graded gap structures. As a result, HgCdTe can be used for detectors operated at various modes [photoconductor, photodiode or metal–insulator–semiconductor (MIS) detector]. At present stage of development of HgCdTe detector technology, the main efforts are directed towards photodiodes due to their compatibility with backside illuminated hybrid FPA technology. Photodiodes with their very low power dissipation, inherently high impedance, negligible $1/f$ noise, and easy multiplexing on focal plane silicon chip, can be assembled in 2D arrays containing a very large number of elements, limited only by existing technologies.

The main motivations to replace HgCdTe are technological problems of this material. One of them is a weak Hg–Te bond, which results in bulk, surface and interface instabilities. Uniformity and yield are still issues especially in the LWIR spectral range. Nevertheless, HgCdTe remains the leading semiconductor for IR detectors.

Since QDIP is an intraband photoconductor and HgCdTe photodiode an interband photovoltaic detector, their fundamental parameters that define detector operation are very different.

4.1. Fundamental figure of merit

4.1.1. Photodiode

Generally, the current gain in a simple photovoltaic detector (e.g., not an avalanche photodiode) is equal to 1, and the magnitude of photocurrent equals

$$I_{ph} = \eta q A \Phi, \tag{12}$$

where η is the quantum efficiency, A is the detector area, and Φ is the photon flux density.

The open-circuit voltage can be obtained by multiplying the short-circuit current by the incremental diode resistance $R = (\partial I/\partial V)^{-1}$ at $V = V_b$

$$V_{ph} = \eta q A \Phi R, \tag{13}$$

where V_b is the bias voltage and $I = f(V)$ is the current–voltage characteristic of the diode.

A frequently encountered figure of merit for IR photodiode is the R_oA product

$$R_oA = \left(\frac{\partial J}{\partial V}\right)^{-1}_{|V_b=0}, \tag{14}$$

where $J = I/A$ is the current density.

For an ideal diffusion-limited diode $I_D = I_s\,[\exp(qV/kT)-1]$, and then

$$R_oA = \frac{kT}{qJ_s} = \frac{kT}{q^2 G_{th} t}, \tag{15}$$

since saturation current density $J_s = qG_{th}t$, where G_{th} is the thermal generation and t is the thickness of the photodiode's active region.

Taking into account Auger 7 mechanism in extrinsic p-type region of n^+-on-p HgCdTe photodiode, we receive

$$(R_oA)_{A7} = \frac{2kT\tau^i_{A7}}{q^2 N_a t} \tag{16}$$

and the same equation for P-on-n photodiode (with dominant contribution of Auger 1 mechanism in n-type region; capital letter means wider gap region)

$$(R_oA)_{A1} = \frac{2kT\tau^i_{A1}}{q^2 N_d t}. \tag{17}$$

where N_a and N_d are the acceptor and donor concentrations in the base regions, respectively; τ^i_{A1} and τ^i_{A7} are the intrinsic Auger 1 and Auger 7 recombination times.

As Eqs. (16) and (17) show, the R_oA product can be decreased by reduction of the thickness of the base layer. Since $\gamma = \tau^i_{A7}/\tau^i_{A1} > 1$, the higher R_oA value can be achieved in p-type base devices compared to that of n-type devices of the same doping level. Detailed analysis shows that the absolute maximum of R_oA is achievable with base layer doping producing $p = \gamma^{1/2} n_i$, which corresponds to the minimum of thermal generation. The required p-type doping is difficult to achieve in practice for low temperature HgCdTe photodiodes (the control of hole concentration below $5 \times 10^{15}\,\mathrm{cm}^{-3}$ level is difficult) and the p-type material suffer from some non-fundamental limitations, such as: contacts, surface and Shockley–Read processes. These are the reasons why the low-temperature detectors are typically produced from the lightly doped n-type materials. Therefore, in further analysis P-on-n photodiodes are considered (P denotes the wider band gap material).

Fig. 9 shows representative characteristics of P-on-n mid-wavelength (MW) HgCdTe photodiode operating at 98 K. The R_oA value is $6.2 \times 10^7\,\Omega\,\mathrm{cm}^2$ at 98 K. The detector is diffusion limited near zero bias, and the dynamic impedance peak at −70 mV reverse bias. Reverse-bias voltages down to −200 mV show no evidence of tunnelling current. Also very good agreement between the measured dark current near zero bias and calculated values can be seen. The dashed line in the figure displays the diffusion slope with an ideality factor equal to 1.13, indicating near diffusion-limited performance.

Since the R_oA product depends on saturation current density [see Eq. (15)], and in turn J_s is determined by the minority carrier lifetime (for HgCdTe ternary alloy τ typically changes in the region between 1 and 10 μs), in the photodiode active region [minority diffusion length $L = (D\tau)^{1/2}$, where D is the diffusion coefficient], so the carrier lifetime

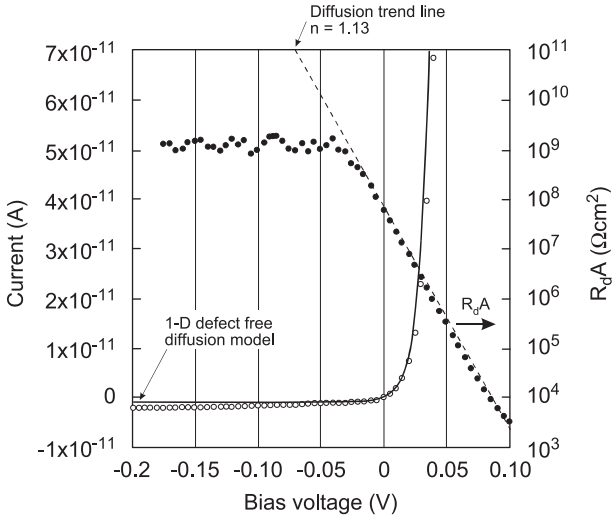

Fig. 9. The I–V characteristic and R_oA product for P-on-n HgCdTe photodiode. Measured cutoff is 4.97 μm at 98 K; the photodiode area is 7.85×10^{-3} cm^{-2}. The dashed line shows the diffusion trend line, which follows the measured data down to ~50 mV, and the solid line the 1-D model that assumes diffusion current from the n-type side (after Ref. [39]).

affects the most important parameters of photodiode: R_oA product and detectivity [see below—Eq. (22)].

The R_oA product is an intrinsic property of the material; it is not possible to increase the detector area without reducing the device resistance. This figure of merit depends on the cutoff wavelength, since λ_c is directly related to the material bandgap. The plots of R_oA data versus temperature generally follow a diffusion current dependence at higher temperatures, and transition into a comparatively temperature-independent tunnelling-like regime at lower temperatures. An example of such behaviour is shown in Fig. 10, where the R_oA product vs. temperature is presented under 0° FOV, for a variety P-on-n $Hg_{1-x}Cd_xTe$ photodiodes made from a range of alloy compositions. The longer wavelength devices are typically more difficult to produce than medium or short wavelength diodes.

The intrinsic noise mechanism of a photodiode is shot noise in the current passing through the diode. It is generally accepted that the noise in an ideal diode is given by

$$I_n^2 = 2q(I_D + 2I_S)\,\Delta f. \tag{18}$$

Photodiodes are typically operated at zero bias to minimize the heat load and for zero $1/f$ noise. In this case

$$I_n^2 = 2(2G + \eta\Phi_B)q^2tA\,\Delta f \tag{19}$$

and the zero bias detectivity can be expressed as

$$D^* = \frac{\eta\lambda q}{hc}\left[\frac{4kT}{R_oA} + 2q^2\eta\Phi_B\right]^{-1/2}. \tag{20}$$

In the last two equations, Φ_B means the total background photon flux density reaching the detector.

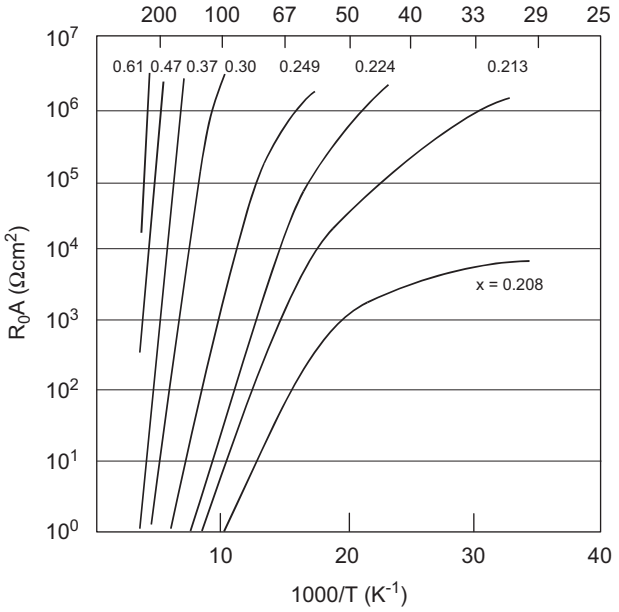

Fig. 10. R_oA product versus temperature for a variety P-on-n $Hg_{1-x}Cd_xTe$ photodiodes made from a range of alloy composition (after Ref. [40]).

For the last formula we may distinguish two important cases:

- background-limited performance; if $4kT/R_oA \ll 2q^2\eta\Phi_B$, then we obtain

$$D^*_{BLIP} = \frac{\lambda}{hc}\left(\frac{\eta}{2\Phi_B}\right)^{1/2}, \tag{21}$$

- thermal noise-limited performance; if $4kT/R_oA \gg 2q^2\eta\Phi_B$, then

$$D^* = \frac{\eta\lambda q}{2hc}\left(\frac{R_oA}{kT}\right)^{1/2}. \tag{22}$$

For the best performance, under the given operation conditions (wavelength, temperature), the value of $\eta(R_oA)^{1/2}$ should be maximized. The $\eta(R_oA)^{1/2}$ is a photodiode figure of merit that determines the performance of a photodiode.

Fig. 11 illustrates the detectivity that can be achieved for P-on-n HgCdTe photodiodes for four selected wavelength regions. At low temperatures, the detector thermal noise is negligible, and detectivity is limited by detector noise due to fluctuations in the arrival rate of photons from room-temperature background radiation (BLIP operation). As detector temperature increases, the detector thermal noise increases exponentially, and usually overcomes the background noise, causing the detectivity to decrease exponentially for further increases in temperature. Detector thermal noise is proportional to the thermal generation rate, which is inversely proportional to the carrier lifetime.

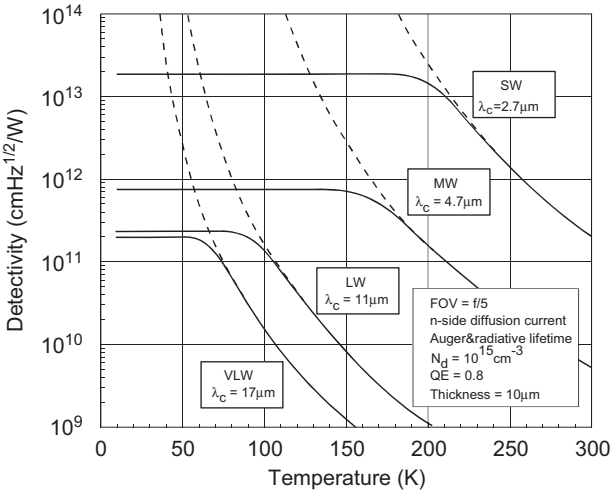

Fig. 11. Calculated detectivity for P-on-n HgCdTe photodiodes for four important wavelength regions, plotted versus operating temperature (after Ref. [41]).

4.1.2. QDIP

Similar with QWIP, the main mechanism producing the dark current in the QDIP device is the thermionic emission of the electrons confined in the quantum dots. The dark current can be given by

$$J_{\text{dark}} = ev n_{3D}, \tag{23}$$

where v is the drift velocity, n_{3D} ($\propto \exp(-E_a/kT)$) is the electron density in the continuum, but E_a is the activation energy, which equals the energy difference between the top of the barrier and the Fermi level in the dot. At higher operating temperature and larger bias voltage, the contribution of field-assisted tunnelling through a triangular potential barrier is considerable [42,43].

Fig. 12 shows, for example, the normalized dark current versus bias for temperature range 20–300 K for QDIP with AlGaAs confinement layers below the QD layer and on top of the GaAs cap layers. In such a case, we have the InAs islands into a quantum wells and AlGaAs blocking layers effectively improve the dark current and detectivity. As it is shown, at low temperature (e.g. 20 K), the dark current increased rapidly as the bias was increased, what is attributed to electron tunnelling between the QDs. For higher bias $|0.2| \leqslant V_{\text{bias}} \leqslant |1.0|$, the dark current increases slowly. With further increase in bias, the dark current strongly increases, what was largely due to lowering of the potential barriers. Fig. 12 also shows the photocurrent induced by the room temperature background. It is clear that BLIP temperature varies with bias.

In contrast to diffusion current of a photodiode, the dark current in a QDIP does not depend on the carrier lifetime, which value typically changes between 100 ps and 1 ns. However, the carrier lifetime is critical in determining the photocurrent, responsivity, and gain.

The basic equation describing photoconductivity is similar to Eq. (12) for photodiode, however, in this additional factor, the photoconductive gain g,

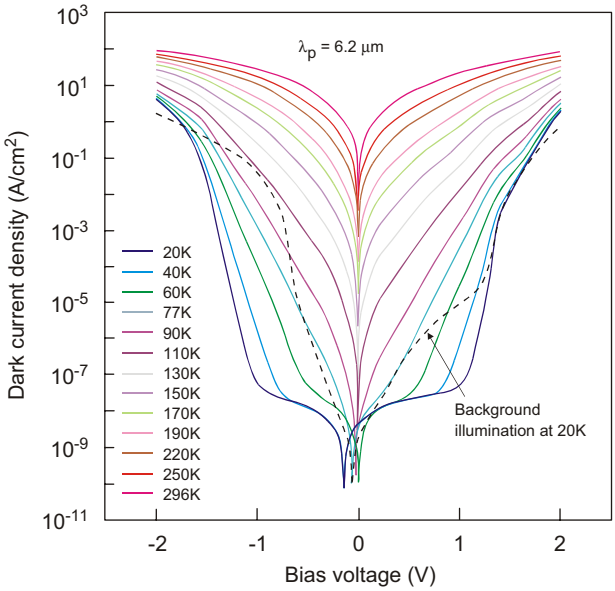

Fig. 12. Dark current density of QDIP with AlGaAs blocking layer including photocurrent induced by room-temperature background (after Ref. [10]).

is included

$$I_{\mathrm{ph}} = \eta q A \Phi g_{\mathrm{ph}}. \tag{24}$$

The photoconductive gain is defined as the ratio of total collected carriers to total excited carriers, whether these carriers are thermally generated or photogenerated. As mentioned previously, in photodiodes typically $g_{\mathrm{ph}} = 1$. However, usually in photoconductors, the gain is greater than 1 since the carrier lifetime τ_{e}, exceeds the carrier transit time τ_{t}, through the device between contacts

$$g_{\mathrm{ph}} = \frac{\tau_{\mathrm{e}}}{\tau_{\mathrm{t}}}. \tag{25}$$

In InAs/GaAs QDIPs, the gain has typical values in the 1–5. However, the gain strongly depends on QDIP design and detector polarization. Much higher values, up to several thousands, have been observed [10,23]. The higher gain of the QDIPs in comparison with QWIPs (typically in the range 0.1–50 for similar electric field intensities) is the result of longer carrier lifetimes.

The larger photoconductive gain has influence on higher current responsivity

$$R_i = \frac{q\lambda}{hc}\eta g_{\mathrm{ph}}. \tag{26}$$

The photoconductive gain and the noise gain in conventional photoconductive detector are equal to each other. It is not the same in QDIPs since these devices are not homogeneous, nor are they bipolar devices. The photoconductive gain in QWIPs is

expressed in terms of the capture probability p_c as [44,45]

$$g_{ph} = \frac{1 - p_c/2}{Np_c}, \tag{27}$$

where $p_c \ll 1$ and N is the number of quantum well layers. This equation is approximately correct for QDs after including the fill factor F, in the denominator that takes into account the surface density of discrete dots across the single layer [46]. Then

$$g_{ph} = \frac{1 - p_c/2}{Np_cF} \tag{28}$$

Ye et al. [47] have estimated an average value of F as equal to 0.35. Recently published paper indicates [48], that temperature-dependent photoresponsivity is attributable to temperature-dependent electron capture probability. The capture probability can be change in wide region, from below 0.01 to above 0.1 in dependence on bias voltage and temperature.

The noise current of QDIP contains both generation-recombination (GR) noise current and thermal noise (Johnson noise) current

$$I_n^2 = I_{n\mathrm{GR}}^2 + I_{n\mathrm{J}}^2 = 4qg_nI_d\,\Delta f + \frac{4kT}{R}\,\Delta f, \tag{29}$$

where R is the differential resistance of the QDIP, which can be extracted from the slope of the dark current.

It can be shown that the noise gain is related to the electron capture probability p_c, as

$$g_n = \frac{1}{Np_cF}. \tag{30}$$

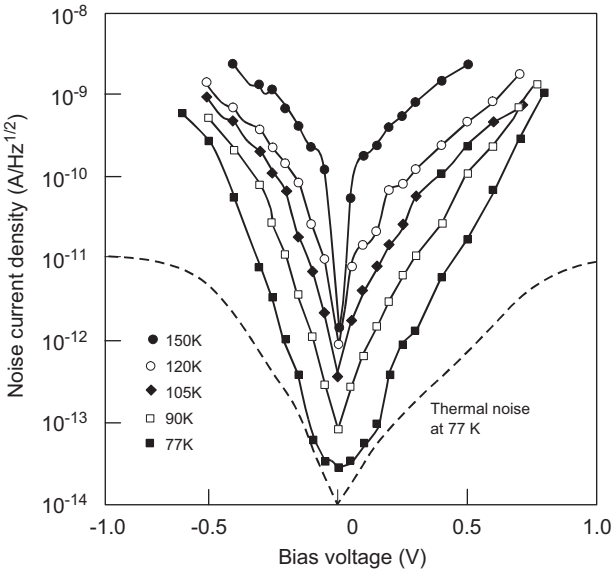

Fig. 13. Noise current density vs. bias voltage at 77, 90, 105, 120, and 150 K. The symbols are measured data. The dashed line is calculated thermal noise current at 77 K (after Ref. [47]).

In typical QDIP, the thermal noise is significant in the very low bias region. For example, Fig. 13 shows the bias dependence of the noise current at 77, 90, 105, 120, and 150 K and a measurement frequency of 140 Hz for InAs/GaAs QDIP. The calculated thermal noise current is also shown at 77 K. Thermal noise is significant in the very low bias region $|V_{\text{bias}}| \leqslant 0.1$ V. As the bias increases, the detector noise current increases much faster than thermal noise and it is primarily GR noise.

Detectivity is defined as the rms signal-to-noise ratio in a 1-Hz bandwidth per unit rms incident radiant power per square root of detector area A_d, and can be determined as

$$D^* = \frac{(A_d\,\Delta f)^{1/2}}{I_n} R_i = \frac{q\lambda}{hc} \frac{\eta g_{ph}}{\left(I_{nGR}^2 + I_{nJ}^2\right)^{1/2}} (A_d\,\Delta f)^{1/2}. \tag{31}$$

4.2. Experimental verification

4.2.1. Performance at low temperature

4.2.1.1. Dark current and R_oA product. In spite of that QDIP is a photoconductor and HgCdTe photodiode, it is interesting to compare their dark currents and incremental resistances. At present stage of technology development, the dark currents of both detectors in the region of low bias voltages are comparable. Fig. 14 displays the dependence of dark currents of 70-layer QDIP [49] and P-on-n HgCdTe photodiode [39] with a peak wavelength of 5 μm. The additional three calculated curves for HgCdTe

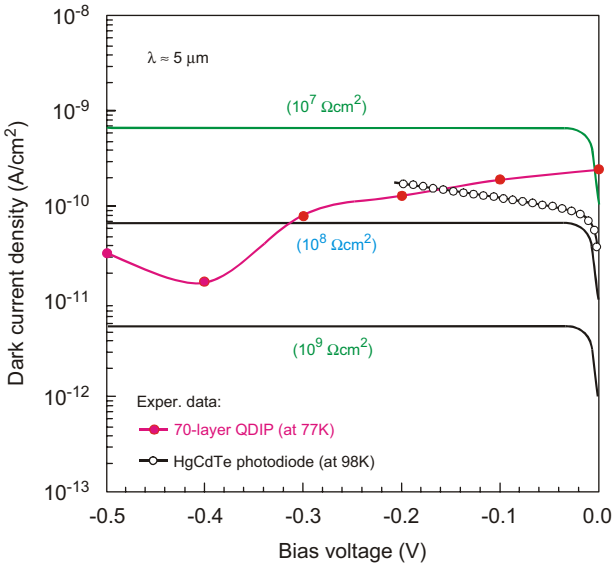

Fig. 14. Comparison of dark currents of 70-layer QDIP (after Ref. [49]) and P-on-n HgCdTe photodiode (after Ref. [39]) with a peak wavelength of 5 μm. The additional three calculated curves for HgCdTe photodiodes are derived from equation $R_oA = kT/qJ_s$ using measured R_oA values from Rockwell Scientific—see Fig. 15 (after Ref. [50]).

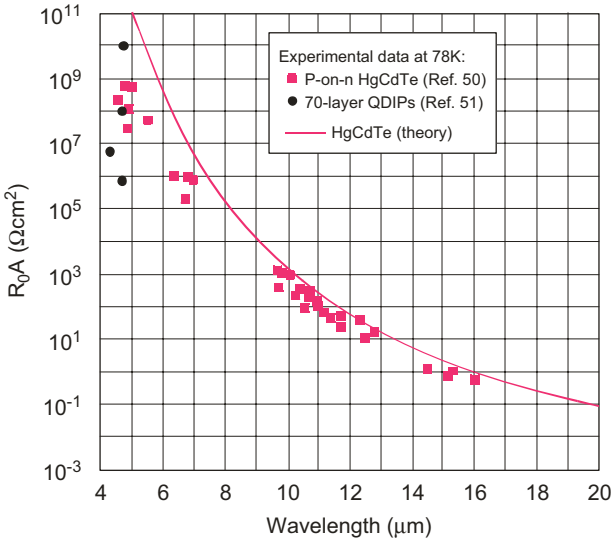

Fig. 15. R_oA vs. wavelength for P-on-n HgCdTe photodiodes and QDIPs at 78 K. Solid line is calculated theoretically assuming 1-D n-side diffusion model.

photodiodes are derived from equation $R_oA = kT/qJ_S$ using measured R_oA values from Rockwell Scientific.

An additional insight into comparison of both types of devices is given in Fig. 15, where the dependence of R_oA product on a wavelength is shown. The QDIP data was determined from dynamic resistance in I–V characteristics at operating bias. Only limited experimental R_oA values for QDIPs marked in Fig. 15 are available in literature [51]. The highest measured R_oA values for HgCdTe photodiodes operated at 78 K with about 5-μm cutoff wavelength are located between 10^8 and $10^9\,\Omega\,cm^2$. The solid line is theoretical R_oA for HgCdTe photodiodes, calculated using a 1-D model that assumes diffusion current from narrower band gap n-side is dominant, and minority carrier recombination via Auger and radiative process. Theoretical calculations used typical values for the n-side donor concentration ($N_d = 1 \times 10^{15}\,cm^{-3}$) and the narrow bandgap active layer thickness (10 μm).

As it was indicated above, the R_oA product is inherent property of the HgCdTe ternary alloy and depends on cutoff wavelength. Dark current of photodiodes increases with cutoff wavelength, what is an important difference with QDIPs, where dark current is far less sensitive to wavelength and depends on device geometry.

4.2.1.2. Detectivity at 78 K. A useful figure of merit, for comparing detector performance, is thermally limited detectivity. In the case of photodiodes, this parameter is defined by Eq. (11). However, for photoconductors the situation is more complicated due to different contribution of thermal noise and GR noise. As it is discussed above, the noise in QDIP originates from the trapping processes in the quantum dots and is more complicated function of detector design and capture probability. As a result, the detectivity depends on several specific quantities, such as the quantum efficiency, photoconductive gain, and contribution of noise current [see Eq. (31)].

Fig. 16 compares the highest measurable detectivities at 77 K of QDIPs found in literature [52–59] with the predicted detectivities of P-on-n HgCdTe and type-II InAs/GaInSb SLS photodiodes. The solid lines are theoretical thermal limited detectivities for HgCdTe photodiodes, calculated using a 1-D model that assumes diffusion current from narrower band gap n-side is dominant, and minority carrier recombination via Auger and radiative process. In calculations of typical values for the n-side donor concentration ($N_d = 1 \times 10^{15}\,cm^{-3}$), the narrow bandgap active layer thickness (10 μm), and quantum efficiency (60%) have been used. It should be insisted, that for HgCdTe photodiodes, theoretically predicted curves for temperature range between 50 and 100 K coincide very well with experimental data (not shown in Fig. 16). The predicted thermally limited detectivities of the type-II SLS are larger than those for HgCdTe [37].

The measured value of QDIPs' detectivities at 77 K gathered in Fig. 16 indicate that QD device detectivities are as yet considerably inferior to current HgCdTe detector performance. In LWIR region, the upper experimental QDIP data at 77 K coincide with HgCdTe ones at temperature 100 K.

4.2.2. Performance at higher temperature

4.2.2.1. Dark current and R_oA product. One of the main potential advantages of QDIPs is low dark current. In particular, the lower dark currents enable higher operating temperatures. Up till now, however, most of the QDIP devices reported in the literature have been working in the temperature range of 77–200 K. On account of this fact, it is interesting to insight on achievable QDIP performance in temperature range above 200 K in comparison with other type of detectors.

Most modern IR devices are fabricated from two pieces of material—a detector array made from compound semiconductor materials and a silicon signal processing chip called a readout integrated circuit (ROIC). The ROIC amplifiers the signal from each detector element and performs processing functions by multiplexing the signals of thousands of pixels onto a few output lines.

The IR arrays have individual-amplifier-per-detector readouts based on metal oxide semiconductor field-effect transistors (MOSFETs). The operating point of the coupled

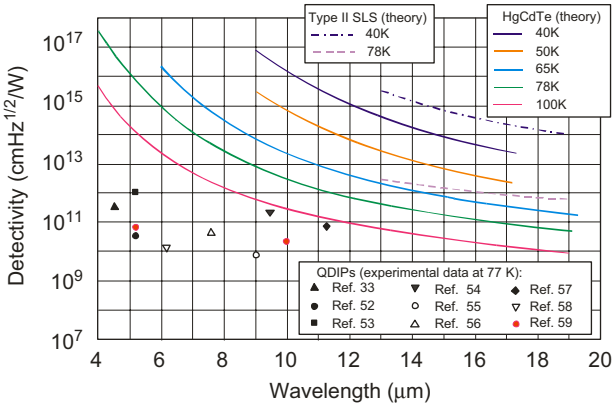

Fig. 16. The predicted detectivity of P-on-n HgCdTe and type-II InAs/GaInSb SLS photodiodes, compared with measured QDIP detectivities at 77 K.

detector and input circuit is found by constructing a load line for the I–V characteristics of the detector and input MOSFET. The input impedance of a MOSFET is a function of the source–drain current (in this case, the total diode current) and is usually expressed in terms of the transconductance, g_m, given by $qI/(nkT)$ for low injected currents (n is an ideality factor that can vary with temperature and geometry of the transistor and usually is in the range 1–2).

The injection efficiency is approximately given by

$$\varepsilon = \frac{IR_d}{IR_d + (nkT/q)}, \tag{32}$$

where R_d is the dynamic impedance of the detector and I is the total injected detector current (the sum of the photocurrent and the dark current) equal photocurrent, I_{ph}, in the background-limited case.

To receive high injection efficiency, the input impedance of the MOSFET must be much lower than the internal dynamic resistance of the detector at its operating point, and the following condition should be fulfilled [60]:

$$IR_d \gg \frac{nkT}{q}. \tag{33}$$

For most applications, the detector performance depends on operating the detector in a small bias where the dynamic resistance is at a maximum. It is then necessary to minimize extraneous leakage current. The control of these leakage currents and the associated low-frequency noise is therefore of crucial interest.

Generally, is not problem to fulfil this inequality for short wavelength infrared (SWIR) and middle wavelength infrared (MWIR) FPAs where the dynamic resistance of detector R_d, is large, but it is very important for LWIR designs where R_d is low. There are more complex injection circuits that effectively reduce the input impedance and allow lower detector resistance to be used.

The above requirement is especially critical for near-room temperature HgCdTe photodetectors operating in LWIR region. Their resistance is very low due to a high thermal generation. In materials with a high electron to hole ration as HgCdTe, the resistance is additionally reduced by ambipolar effects. Small size uncooled 10.6-μm photodiodes ($50 \times 50\,\mu m^2$) exhibit less than $1\,\Omega$ zero bias junction resistances which are well below the series resistance of a diode. As a result, the performance of conventional devices is very poor, so they are not usable for practical applications. To fulfil inequality (33) to effectively couple the detector with silicon readout, the detector incremental resistance should be $R_d \gg 2\,\Omega$. As Fig. 17 shows, the saturation current for 10-μm photodiode achieves $1000\,A/cm^2$ and it is by four orders of magnitude larger than the photocurrent due to the 300 K background radiation. The potential advantages of QDIPs is considerably lower dark current and higher R_oA product in comparison with HgCdTe photodiodes (see Fig. 18).

4.2.2.2. Detectivity at room temperature. Fig. 19 compares the calculated thermal detectivity of HgCdTe photodiodes and QDIPs as a function of wavelength and operating temperature with the experimental data of uncooled HgCdTe and type-II InAs/GaInSb SLS detectors. The Auger mechanism is likely to impose fundamental limitations to the LWIR HgCdTe detector performance. The calculations

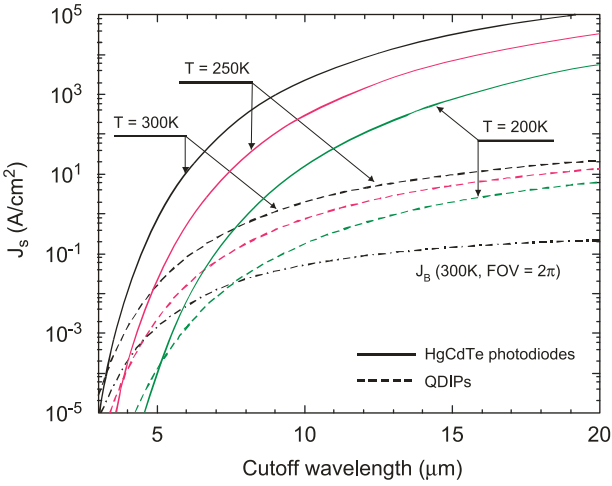

Fig. 17. Dark current density of HgCdTe photodiodes and QDIPs, and background-generated photocurrent as a function of wavelength. The calculations for HgCdTe photodiodes have been performed for the optimized doping concentration $p = \gamma^{1/2} n_i$.

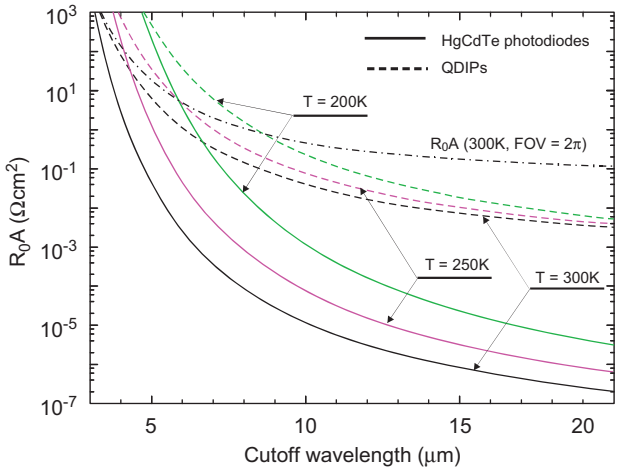

Fig. 18. R_oA product of HgCdTe photodiodes and QDIPs as a function of wavelength. The calculations for HgCdTe photodiodes have been performed for the optimized doping concentration $p = \gamma^{1/2} n_i$.

have been performed for optimized doping concentration $p = \gamma^{1/2} n_i$. The experimental data for QDIPs are gathered from the literature for detectors operated at 200 and 300 K.

Uncooled LWIR HgCdTe photodetectors are commercially available and manufactured in significant quantities, mostly as single-element devices [61–63]. They have found important applications in IR systems that require fast response. The results presented in Fig. 19 confirm that the type-II superlattice is a good candidate for IR detectors operating in the spectral range from the mid-wavelength to the very long-wavelength IR. However,

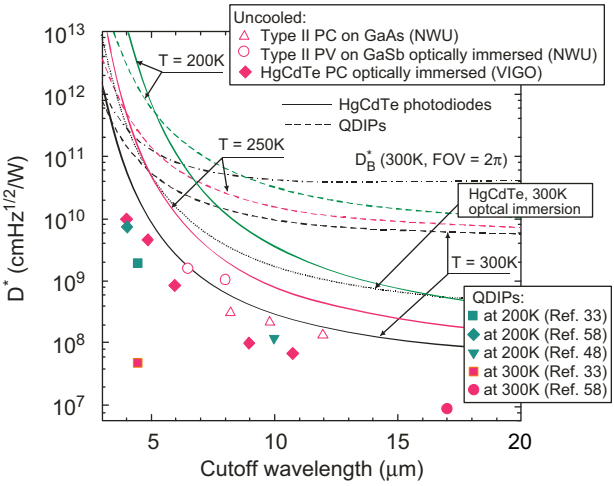

Fig. 19. Calculated performance of Auger generation-recombination limited HgCdTe photodetectors as a function of wavelength and operating temperature. BLIP detectivity has been calculated for 2π FOV, the background temperature is $T_{BLIP} = 300\,K$, and the quantum efficiency $\eta = 1$. The calculations for HgCdTe photodiodes have been performed for the optimized doping concentration $p = \gamma^{1/2} n_i$. The experimental data is taken for commercially available uncooled HgCdTe photoconductors (produced by Vigo System) and uncooled type-II detectors at the Center for Quantum Devices, Northwestern University (US). The experimental data for QDIPs are gathered from the marked literature for detectors operated at 200 and 300 K.

comparison of QDIP performance both with HgCdTe and type-II superlattice detectors gives clear evidence that the QDIP is suitable for high temperature. Especially encouraging results have been achieved for very long-wavelength QDIP devices with a double-barrier resonant tunnelling filter with each quantum-dot layer in the absorption region [64,65]. In this type of devices, photoelectrons are selectively collected from the QDs by resonant tunnelling, while the same tunnel barriers block electrons of dark current due to their broad energy distribution. For the 17-μm detector, a peak detectivity of 8.5×10^6 cm $Hz^{1/2}$/W has been measured. Up till now, this novel device demonstrates the highest performance of room-temperature photodetectors. Further improvement in technology and design can result in application of QDIPs in room temperature FPAs with the advantages of larger operating speed (shorter frame time) in comparison with thermal detectors (bolometers and pyroelectric devices).

The room-temperature operation of thermal detectors makes them lightweight, rugged, reliable, and convenient to use. However, their performance is modest, and they suffer from slow response. Because they are nonselective detectors, their imaging systems contain very broadband optics, which provide impressive sensitivity at a short range in good atmospheres.

Thermal detectors seem to be unsuitable for the next generation of IR thermal imaging systems, which are moving toward faster frame rates and multispectral operation. A response time much shorter than that achievable with thermal detectors is required for many nonimaging applications. Improvement in technology and design of QDIP detectors make it possible to achieve both high sensitivity and fast response at room temperature.

5. Conclusions

The intention of this paper was to compare the achievements of QDIP technology with those of competitive technologies, with the emphasis on the material properties, device structure, and their impact on the device performance, especially in LWIR spectral regions.

At present, HgCdTe is the most widely used variable-gap semiconductor that has a privileged position both in the MWIR as well as LWIR spectral ranges. Theoretical predictions indicate that only type-II superlattice photodiodes and QDIPs are expected to compete with HgCdTe photodiodes. However, the measured values of QDIPs' detectivities at 77 K are considerably inferior to current HgCdTe detector performance. Improving QD uniformity is a key issue in the increasing the absorption coefficient and improving the performance.

Poor QDIP performance is generally linked to two sources: nonoptimal band structure and nonuniformity in QD size. In the paper, an ideal QD structure is analysed theoretically (with two-electron energy levels, where the excited state coincides with the conduction band minimum of the barrier material). If the excited state is below the barrier conduction band, photocurrent is difficult to extract. Also usually, QDs contain additional energy levels between the excited and ground state transitions. If these states are similar to the thermal excitations or permit phonon scattering between levels, carrier lifetime is dramatically reduced. In consequence a large increase in dark current and reduction in detectivity are observed. It should be also noticed that in the case of Stranski–Krastanow growth mode a some degradation of self-assembled QDs occur due to a coupling 2D "wetting layer".

Comparison of QDIP performance both with HgCdTe and type-II superlattice detectors gave clear evidence that the QDIP is suitable for high operation temperature. Especially encouraging results have been recently achieved for very long-wavelength QDIP devices with a double-barrier resonant tunnelling filter. Due to fact that conventional HgCdTe photodiodes are not usable for room temperature FPA applications, it can be expected that improvement in technology and design of QDIP detectors will make it possible to achieve both high sensitivity and fast response useful for practical application in room temperature FPAs. This new generation of room temperature FPAs will eventually compete with silicon microbolometers, dominant at present. Larger operating speed of QDIP and multispectral capability are considerable advantages in comparison with thermal detectors.

Optimization of the QDIP architecture is still an open area. Since some of the design parameters depend on a device structure (photoconductive and noise gains, dark current, quantum efficiency), the performance is still being improved.

Appendix A

A.1. HgCdTe

Properties of HgCdTe photodiodes are determined by minority carriers. In thermal equilibrium

$$n_{\min} = \frac{n_i^2}{n_{\mathrm{maj}}}, \tag{A.1}$$

where n_i is the intrinsic carrier concentration, and n_{maj} is the majority carrier concentration.

The Auger mechanism is more likely to impose fundamental limitations to the LWIR HgCdTe detector performance [66,67]. In this case, the minority carrier lifetime is equal to

$$\tau_{min} = 2\tau_{Ai}\frac{n_i^2}{n_{maj}(n_{maj}+n_{min})}, \tag{A.2}$$

where τ_{Ai} is the Auger lifetime for intrinsic material.

The thermal generation rate associated with Auger mechanism can be described as [see Eq. (4)]

$$G_{th} = \frac{n_{min}}{\alpha\tau_{min}} = \frac{n_{maj}}{2\alpha\tau_{Ai}}. \tag{A.3}$$

It is well known that Auger 1 process is decisive in n-type HgCdTe. Then, the intrinsic Auger 1 lifetime can be approximated by [66]

$$\tau_{Ai1} = 8.3\times10^{-13}E_g^{1/2}\left(\frac{q}{kT}\right)^{3/2}\exp\left(\frac{qE_g}{kT}\right), \tag{A.4}$$

where E_g is in eV. Assuming further that absorption coefficient, α is equal to $10^3\,cm^{-1}$, the thermal generation rate is given by [5]

$$G_{th} = 4.8\times10^2\frac{n_{maj}T^{3/2}}{E_g^{1/2}\exp(qE_g/kT)}\ (\text{in cm}^2/\text{s}) \tag{A.5}$$

The above-described procedure can be used for p-type HgCdTe changing only Auger 1 mechanism on Auger 7, which is decisive in p-type material. It is expected that Auger 7 process is weaker than Auger 1, since $\gamma = \tau^i_{A7}/\tau^i_{A1} > 1$ [68]. Higher recombination lifetimes are expected in p-type materials compared to n-type materials of the same doping.

A.2. QWIP

Let us consider n-type QWIP with a bound-to-bound operation. It is not the most commonly used QWIP architecture, but it does serve to illustrate most simply limitations of this concept [69]. If in thermal equilibrium the ground is filled with n_o electrons, the Fermi level is

$$E_F = \frac{n_o h^2 d}{4\pi m^*}, \tag{A.6}$$

where d is the well width. Typical values of n_o are between 2×10^{17} and $2\times10^{18}\,cm^{-3}$.

The carrier concentration in the second level can be determined by Fermi energy and the density of states in the second level

$$n_2 = n_o\left(\frac{kT}{qE_F}\right)\exp\left[\frac{q(E_F-E_2)}{kT}\right]. \tag{A.7}$$

Optical selection rule for interband absorption allows transitions only for E-field polarization vectors normal to detector surface. In such situation we assume the

unpolarized absorption coefficient for the GaAs active layers as [70]

$$\alpha \approx 5 \times 10^{-15} n_o \text{ (in cm}^{-1}\text{)} \tag{A.8}$$

and the maximum absorption quantum efficiency of 50%, due to the unpolarized nature of the incident radiation.

To estimate the thermal generation rate of the QWIP, the thickness of the active volume of detector equal to $1/\alpha$, and carrier lifetime $\tau = 10$ ps (typical estimated values are between 1 and 10 ps) have been chosen. According to Eq. (4)

$$G_{th} = 2 \times 10^{25} \left(\frac{kT}{qE_F}\right) \exp\left[\frac{q(E_F - E_2)}{kT}\right]. \tag{A.9}$$

G_{th} assumes minimal value when $E_F = kT/q$, and then [5]

$$G_{th} = 5.5 \times 10^{25} \exp\left[-\frac{qE_g}{kT}\right] \text{ (in cm}^2\text{/s)}, \tag{A.10}$$

where $E_g = E_2 - E_1$ (in eV).

A.3. Photoemissive detectors

Silicon Schottky barrier photoemissive detectors belong to majority carrier devices. Radiation is transmitted through the p-type silicon and is absorbed in the metal PtSi (not in the semiconductor), producing hot holes, which are then emitted over the potential metal/semiconductor barrier into the silicon, leaving the silicide charged negatively. In monolithic FPAs, the negative charge of silicide is transferred to silicon readout by the direct charge injection method.

The thermal carrier density at the barrier is obtained by integration over the density of states. It can be shown that

$$\begin{aligned} n_o &= 8\pi m^{3/2} kT[2(E_F + E_g)]^{1/2} h^3 \exp\left(-\frac{qE_g}{kT}\right) \\ &= 2 \times 10^{18} T \exp\left(-\frac{qE_g}{kT}\right), \end{aligned} \tag{A.11}$$

where $E_F - E_g \approx 8$ eV [71]. As previously, E_g is the barrier height (in eV).

The carrier lifetime in metal is determined by carrier–carrier scattering and can be estimated as [72]

$$\tau \approx \frac{1.5 \times 10^{-14}}{E_g^2} \text{ (in s)}, \tag{A.12}$$

where E_g is in eV.

To enhance radiation coupling with detector, usually the resonant structures are used with a thickness of active region between 1 and 2 nm, yielding an absorption efficiency of 0.3 [71]. Assuming detector thickness of 1.5 nm, it can be obtained [5]

$$G_{th} = \frac{n_o t}{\tau} = 2 \times 10^{25} T E_g^2 \exp\left(-\frac{qE_g}{kT}\right) \text{ (in cm}^2\text{/s)}. \tag{A.13}$$

A.4. Extrinsic detectors

At the low temperature of operation of impurity photoconductors (when $kT \ll E_d$ and $n \ll N_d$, N_a), the thermal equilibrium free-charge carrier in a n-type extrinsic semiconductor with a partially compensated singly iodized level is equal to [73,74],

$$n_{th} = n_{maj} = \frac{N_c}{2}\left(\frac{N_d - N_a}{N_a}\right)\exp\left(-\frac{E_d}{kT}\right). \tag{A.14}$$

Here N_c is the density of states in the conduction band, N_d is the donor concentration, N_a is the compensating acceptor concentration, and E_d is the bonding energy of the donor relative to the conduction band.

The majority carrier lifetime is determined by the density of empty (ionized) donor levels, and for low temperatures, such that $n_{maj} < N_a < N_d$, is given by

$$\tau = (\sigma_c v_{th} N_a)^{-1}, \tag{A.15}$$

where σ_c is the capture cross-section for electrons into the donor level, and $v_{th} = (8kT/\pi m^*)^{1/2}$ is the carrier thermal velocity. For shallow-level impurities (B and As) typically, $\sigma_c \approx 10^{-11}\,\mathrm{cm}^2$, while for the deep-level impurities (In, Au, Zn) show, $\sigma_c = 10^{-13}\,\mathrm{cm}^2$ (by comparison, the σ_c of intrinsic photoconductors is about $10^{-17}\,\mathrm{cm}^2$) [74].

The absorption coefficient can be estimated by [75]

$$\alpha = 10^{-15} n_{maj}\ (\text{in cm}^{-1}) \tag{A.16}$$

with n_{maj} in cm^{-3}.

Assuming above-described relations, $\sigma_c = 10^{-13}\,\mathrm{cm}^2$, and the effective mass $m^* = 0.4m_o$, the thermal generation rate is

$$G_{th} = 3 \times 10^{23} T^{3/2} \exp\left(-\frac{qE_d}{kT}\right)\ (\text{in cm}^2/\text{s}). \tag{A.17}$$

A.5. High-temperature superconductor (HTSC)

The HTSC detectors considered here are treated as the photon detectors in which optical excitation takes place across the superconducting energy gap $E_g = 2\Delta$. According to Bardeen–Cooper–Schrieffer theory, the value of 2Δ is given by $3.53kT_c$, where T_c is the critical temperature. For a transition temperature of 90 K (typical for YbaCuO), the energy gap predicted by this relation is 27 meV [76].

The density of quasiparticles in a superconductor is given by [77]

$$n_t = 2N_o(\pi E_g kT)^{1/2} \exp\left(-\frac{E_g}{2kT}\right), \tag{A.18}$$

where N_o is the single spin density of states at the Fermi level at $T = 0$.

The analysis of recombination lifetime in supeconductors indicates on dominant contribution of electron–phonon interactions. Discussion carried out by Rothwarth and Taylor shows that the effective quasiparticle lifetime can be approximated by the following equation [78]:

$$\tau_{eff} = \frac{\beta n_t t}{8N_{\omega t} s}, \tag{A.19}$$

where $N_{\omega t}$ is the equilibrium density of phonons with the energy $h\omega/2\pi > 2\Delta$, s is the velocity of sound ($\approx 3 \times 10^5$ cm/s) and $\beta > 1$. Assuming that the device thickness is in the range 20–100 nm, the thermal generation rate of quasiparticles is [5]

$$G_{\text{th}} = 4 \times 10^{41} \frac{TE_{\text{g}}^2}{\beta s^2} \exp\left(-\frac{qE_{\text{g}}}{kT}\right). \tag{A.20}$$

References

[1] L. Esaki, R. Tsu, IBM J. Res. Dev. 14 (1970) 61.
[2] Y. Arakawa, H. Sakaki, Appl. Phys. Lett. 40 (1982) 939.
[3] M. Asada, Y. Miyamoto, Y. Suematsu, IEEE J. Quantum Electron. QE-22 (1986) 1915.
[4] D. Bimberg, M. Grundmann, N.N. Ledentsov, Quantum Dot Heterostructures, Wiley, Chichester, 1999.
[5] M.A. Kinch, J. Electron. Mater. 29 (2000) 809.
[6] Ch. Sikorski, U. Merkt, Phys. Rev. Lett. 62 (1989) 2164.
[7] T. Demel, D. Heitmann, P. Grambow, K. Ploog, Phys. Rev. Lett. 64 (1990) 788.
[8] J. Phillips, K. Kamath, Bhattacharya, Appl. Phys. Lett. 72 (1998) 2020.
[9] P. Bhattacharya, Z. Mi, Proc. IEEE 95 (2007) 1723.
[10] J.C. Campbell, A. Madhukar, Proc. IEEE 95 (2007) 1815.
[11] S. Krishna, S.D. Gunapala, S.V. Bandara, C. Hill, D.Z. Ting, Proc. IEEE 95 (2007) 1838.
[12] D. Leonard, M. Krishnamurthy, C.M. Reaves, S.P. Denbaars, P.M. Petroff, Appl. Phys. Lett. 63 (1993) 3203.
[13] I.N. Stranski, L. Krastanow, Sitzungsber. Akad. Wiss. Wein Abt. IIb 146 (1937) 797.
[14] S.D. Gunapala, S.V. Bandara, GaAs/AlGaAs based quantum well infrared photodetector focal plane arrays, in: M. Henini, M. Razeghi (Eds.), Handbook of Infrared Detection Technologies, Elsevier, Oxford, 2002, pp. 83–119.
[15] A. Rogalski, J. Appl. Phys. 93 (2003) 4355.
[16] J. Phillips, J. Appl. Phys. 91 (2002) 4590.
[17] H.C. Liu, Opto-Electron. Rev. 11 (2003) 1.
[18] S.Y. Wang, S.D. Lin, W. Wu, C.P. Lee, Appl. Phys. Lett. 78 (2001) 1023.
[19] V. Ryzhii, J. Appl. Phys. 89 (2001) 5117.
[20] S. Krishna, J. Phys. D: Appl. Phys. 38 (2005) 2142.
[21] S.D. Gunapala, S.V. Bandara, C.J. Hill, D.Z. Ting, J.K. Liu, B. Rafol, E.R. Blazejewski, J.M. Mumolo, S.A. Keo, S. Krishna, Y.-C. Chang, C.A. Shott, IEEE J. Quantum Electron. 43 (2007) 230.
[22] S.W. Lee, K. Hirakawa, Y. Shimada, Appl. Phys. Lett. 75 (1999) 1428.
[23] I. Vurgaftman, Y. Lam, J. Singh, Phys. Rev. B 50 (1994) 14309.
[24] E. Towe, D. Pan, IEEE J. Sel. Top. Quantum Electron. 6 (2000) 408.
[25] D. Long, Photovoltaic and photoconductive infrared detectors, in: R.J. Keyes (Ed.), Optical and Infrared Detectors, Springer, Berlin, 1977, pp. 101–147.
[26] C.T. Elliott, N.T. Gordon, Infrared detectors, in: C. Hilsum (Ed.), Handbook on Semiconductors, vol. 4, North-Holland, Amsterdam, 1993, pp. 841–936.
[27] C.T. Elliott, C.L. Jones, Non-equilibrium devices in HgCdTe, in: P. Capper (Ed.), Narrow-Gap II–VI Compounds for Optoelectronic and Electromagnetic Applications, Chapman & Hall, London, 1997, pp. 474–485.
[28] J. Piotrowski, W. Gawron, Infrared Phys. Technol. 38 (1997) 63.
[29] P.N. Brounkov, A. Polimeni, S.T. Stoddart, M. Henini, L. Eaves, P.C. Main, A.R. Kovsh, Yu.G. Musikhin, S.G. Konnikov, Appl. Phys. Lett. 73 (1998) 1092.
[30] H. Jiang, J. Singh, IEEE J. Quantum Electron. 34 (1998) 1188.
[31] A. Rogalski, K. Adamiec, J. Rutkowski, Narrow-Gap Semiconductor Photodiodes, SPIE Press, Bellingham, 2000.
[32] A. Rogalski, Rep. Prog. Phys. 68 (2005) 2267.
[33] H. Lim, S. Tsao, W. Zhang, M. Razeghi, Appl. Phys. Lett. 90 (2007) 131112.
[34] D.L. Smith, C. Mailhiot, J. Appl. Phys. 62 (1987) 2545.

[35] C.H. Grein, P.M. Young, H. Ehrenreich, Appl. Phys. Lett. 61 (1992) 2905.
[36] E.R. Youngdale, J.R. Meyer, C.A. Hoffman, F.J. Bartoli, C.H. Grein, P.M. Young, H. Ehrenreich, R.H. Miles, D.H. Chow, Appl. Phys. Lett. 64 (1994) 3160.
[37] C.H. Grein, H. Cruz, M.E. Flatte, H. Ehrenreich, Appl. Phys. Lett. 65 (1994) 2530.
[38] C.H. Grein, P.M. Young, M.E. Flatté, H. Ehrenreich, J. Appl. Phys. 78 (1995) 7143.
[39] P.S. Wijewarnasuriya, M. Zandian, J. Phillips, D. Edwall, R.E. DeWames, G. Hildebrandt, J. Bajaj, J.M. Arias, A.I. D'Souza, F. Moore, J. Electron. Mater. 31 (2002) 726.
[40] P. Norton, Opto-Electron. Rev. 10 (2002) 159.
[41] M.B. Reine, Fundamental properties of mercury cadmium telluride, in: Encyclopedia of Modern Optics, Academic Press, London, 2004.
[42] J.-Y. Duboz, H.C. Liu, Z.R. Wasilewski, M. Byloss, R. Dudek, J. Appl. Phys. 93 (2003) 1320.
[43] A.D. Stiff-Roberts, X.H. Su, S. Chakrabarti, P. Bhattacharya, IEEE Photon. Technol. Lett. 16 (2004) 867.
[44] H.C. Liu, Appl. Phys. Lett. 61 (1992) 2703.
[45] W.A. Beck, Appl. Phys. Lett. 63 (1993) 3589.
[46] J. Phillips, P. Bhattacharya, S.W. Kennerly, D.W. Beekman, M. Duta, IEEE J. Quantum Electron. 35 (1999) 936.
[47] Z. Ye, J.C. Campbell, Z. Chen, E.T. Kim, A. Madhukar, Appl. Phys. Lett. 83 (2003) 1234.
[48] X. Lu, J. Vaillancourt, M.J. Meisner, Appl. Phys. Lett. 91 (2007) 051115.
[49] P. Bhattacharya, S. Chakrabarti, X. Su, A.D. Stiff-Roberts, Laser Focus World 41 (2005) 103.
[50] T. Chuh, Proc. SPIE 5563 (2004) 19.
[51] P. Bhattacharya, A.D. Stiff-Roberts, S. Chakrabarti, Mid-infrared quantum dot photoconductors, in: A. Krier (Ed.), Mid-infrared Semiconductor Optoelectronics, Springer, Berlin, 2007, pp. 487–513.
[52] J. Jiang, S. Tsao, T. O'Sullivan, W. Zhang, H. Lim, T. Sills, K. Mi, M. Razeghi, G.J. Brown, M.Z. Tidrow, Appl. Phys. Lett. 84 (2004) 2166.
[53] J. Szafraniec, S. Tsao, W. Zhang, H. Lim, M. Taguchi, A.A. Quivy, B. Movaghar, M. Razeghi, Appl. Phys. Lett. 88 (2006) 121102.
[54] E.-T. Kim, A. Madhukar, Z. Ye, J.C. Campbell, Appl. Phys. Lett. 84 (2004) 3277.
[55] S.D. Gunapala, S.V. Bandara, C.J. Hill, D.Z. Ting, J.K. Liu, B. Rafol, E.R. Blazejewski, J.M. Mumolo, S.A. Keo, S. Krishna, Y.-C. Chang, C.A. Shott, IEEE J. Quantum Electron. 43 (2007) 230.
[56] S. Chakrabarti, X.H. Su, P. Bhattacharya, G. Ariyawansa, A.G.U. Perera, IEEE Photon. Technol. Lett. 17 (2005) 178180.
[57] R.S. Attaluri, S. Annamalai, K.T. Posani, A. Stintz, S. Krishna, J. Vac. Sci. Technol. B 24 (2006) 1553.
[58] S. Chakrabarti, A.D. Stiff-Roberts, X.H. Su, P. Bhttacharya, G. Ariyawansa, A.G.U. Perera, J. Phys. D: Appl. Phys. 38 (2005) 2135.
[59] S. Krishna, D. Forman, S. Annamalai, P. Dowd, P. Varangis, T. Tumolillo, A. Gray, J. Zilko, K. Sun, M. Liu, J. Campbell, D. Carothers, Phys. Status Solidi (c) 3 (2006) 439.
[60] J.L. Vampola, Readout electronic for infrared sensors, in: W.D. Rogatto (Ed.), The Infrared and Electro-Optical Systems Handbook, vol. 3, SPIE Optical Engineering Press, Bellingham, 1993, pp. 285–342.
[61] J. Piotrowski, A. Rogalski, Infrared Phys. Technol. 46 (2004) 115.
[62] Vigo System, ⟨www.vigo.com.pl⟩.
[63] J. Piotrowski, A. Rogalski, High-operating Temperature Infrared Photodetectors, SPIE Press, Bellingham, 2007.
[64] X.H. Su, S. Chakrabarti, P. Bhattacharya, A. Ariyawansa, A.G.U. Perera, IEEE J. Quantum Electron. 41 (2005) 974.
[65] A.G.U. Perera, G. Ariyawansa, V.M. Apalkov, S.G. Matsik, X.H. Su, S. Chakrabarti, P. Bhattacharya, Opto-Electron. Rev. 15 (2007) 223.
[66] M.A. Kinch, M.J. Brau, A. Simmons, J. Appl. Phys. 44 (1973) 1649.
[67] P.E. Petersen, Auger recombination in mercury cadmium telluride, in: R.K. Willardson, A.C. Beer (Eds.), Semiconductors and Semimetals, vol. 18, Academic Press, New York, 1981, pp. 121–155.
[68] T.N. Casselman, J. Appl. Phys. 52 (1981) 848.
[69] M.A. Kinch, A. Yariv, Appl. Phys. Lett. 55 (1989) 2093.
[70] B.F. Levine, C.G. Bethea, G. Hasnain, J. Walker, R.J. Malik, Appl. Phys. Lett. 53 (1988) 296.
[71] D.E. Mercer, C.R. Helms, J. Appl. Phys. 65 (1989) 5035.
[72] J.J. Quinn, Phys. Rev. 126 (1962) 1453.
[73] P.R. Bratt, Impurity germanium and silicon infrared detectors, in: R.K. Willardson, A.C. Beer (Eds.), Semiconductors and Semimetals, vol. 12, Academic Press, New York, 1977, pp. 39–141.

[74] N. Sclar, Prog. Quantum Electron. 9 (1984) 149.
[75] Y. Darviot, A. Sorrentino, B. Joly, B. Pajot, Infrared Phys. 7 (1967) 1.
[76] A. Rogalski, Infrared Detectors, Gordon & Breach, Amsterdam, 2000.
[77] W.H. Parker, W.D. Williams, Phys. Rev. Lett. 29 (1972) 924.
[78] A. Rothwarf, B.N. Taylor, Phys. Rev. Lett. 19 (1967) 27.